Supplementary Information

Real-time Crystallographic Capture of Fe–NO Bond Photodissociation in a Nonheme Iron Nitrosyl Complex

Seungwon Sun[1,6], Sangho So[3,4,6], Dohyun Moon[5]*, Mu-Hyun Baik[3,4]* and Jaeheung Cho[1,2]*

[1]Department of Chemistry, Ulsan National Institute of Science and Technology (UNIST), Ulsan 44919, Republic of Korea

[2]Graduate School of Carbon Neutrality, Ulsan National Institute of Science and Technology (UNIST), Ulsan 44919, Republic of Korea.

[3]Department of Chemistry, Korea Advanced Institute of Science and Technology (KAIST), Daejeon 34141, Republic of Korea

[4]Center for Catalytic Hydrocarbon Functionalizations, Institute for Basic Science (IBS), Daejeon 34141, Republic of Korea

[5]Beamline Department, Pohang Accelerator Laboratory, Pohang, Gyeongbuk 37673, Republic of Korea

[6]These authors contributed equally to this work

*Corresponding authors: jaeheung@unist.ac.kr, mbaik2805@kaist.ac.kr, dmoon@postech.ac.kr

Table of contents

I. General experimental details

Materials. All reagents and solvents were commercially available from Sigma-Aldrich, TCI, Fisher Scientific, or BOC Science and used without further purification unless otherwise indicated. The diethyl ether (Et_2O) was purified through solvent purification columns (JC Meyer Solvent Systems) prior to use. The *N,N*'-di-*tert*-butyl-2,11-diaza[3.3](2,6)-*p*-chloro-pyridinophane (Cl−TBDAP) was synthesized according to the literature procedures[1].

Instrumentation. UV-vis spectra were recorded on a Cary 8454 diode array spectrophotometer equipped with an UNISOKU Scientific Instruments Cryostat USP-203 for –40 °C. Mass spectrometry was performed on electrospray ionization mass spectrometry (ESI-MS, Waters, Acquity SQD quadrupole Mass instrument, detailed parameter: spray voltage; 2.5 kV, capillary temperature; 80 °C), and on cold spray ionization mass spectrometry (CSI-MS, JEOL, JMS-T1000LP 4G, detailed parameter: spray voltage; 2.0 kV, capillary temperature; 40 °C). Infrared (IR) vibrational spectra were recorded on a Thermo Scientific Nicolet iS10 equipped with a diamond attenuated total reflectance (ATR) accessory. X-band continuous wave electron paramagnetic resonance (CW-EPR) spectrum was taken at 100 K using a Bruker EMXplus spectrometer equipped with a dual-mode resonator (ER 4116DM). The low temperature was achieved and controlled with the digital temperature and gas flow control system (ER 4141VT). The experimental parameters for EPR measurement were as follows: Microwave frequency = 9.422 GHz, microwave power = 1.0 mW, modulation amplitude = 5 G, gain = 1.59×10^4, modulation frequency = 100 kHz, time constant = 327.68 ms, and conversion time = 100 ms. ^{1}H-NMR spectra were measured with an NMR spectrometer (Varian, VNMRS600). Xenon lamp (Asahi Spectra, Max-303, 300 W) was used as a light source for releasing NO$^\bullet$ from **2** experiments, and the power of the light (at 532 nm) was measured by using an Economical Handheld Laser Power Meter (Newport, 843-R).

Magnetic moment measurement. The effective magnetic moments were determined by the ^{1}H NMR Evans method at –40 °C for **2**[2,3]. A WILMAD® coaxial insert (sealed capillary) tube containing the blank acetone-d_6 solvent (with 0.03% TMS) only was inserted into the normal NMR tube containing the complexes (3 mM) dissolved in acetone-d_6 (with 0.03% TMS). The chemical shift of the TMS peak (and/or solvent peak) in the presence of the paramagnetic metal complexes was compared to that of the TMS peak (and/or solvent peak) in the inner coaxial insert tube. The effective magnetic moments were calculated using the equation, $\mu_{\text{eff}} = 0.0618(\Delta vT/2fM)^{1/2}$, where f is the oscillator frequency (MHz) of the superconducting spectrometer, T is the absolute temperature, M is the molar concentration of the metal ion, and $\Delta\nu$ is the difference in frequency (Hz) between the two reference signals.

Purification of nitric oxide. Nitric oxide (NO$^\bullet$) gas was purchased from Korea Standard Gas and purified as follows: NO$^\bullet$ was passed through two columns filled with NaOH beads and molecular sieves and collected in frozen form in a trap cooled at 77 K with liquid N_2[4,5]. Frozen NO$^\bullet$ was warmed up to 193 K (Ethanol/dry-ice mixture, –80 °C), and the highly purified NO$^\bullet$ was added to the sample in a Schlenk flask fitted with a rubber septum (free from oxygen, after several cycles of vacuum and N_2 purging).

Photodissociation reaction studies. Photolysis of **2** and $[Fe(TBDAP)(NO)(H_2O)]^{2+}$ (2 mM) was performed in acetone at –40 °C upon photo-illumination. Broadband light from a xenon lamp was employed as a photon source. The progress of photolysis was monitored by employing UV–vis absorption spectrophotometer. The sample was delivered into a quartz cuvette (beam path length = 1 cm) under aerobic conditions, and UV–vis absorption spectra were recorded during photo-illumination. The xenon lamp was positioned at a distance of ~4.2 cm from the quartz cuvette 90° to the UV–vis beam. All photolysis experiments were carried

out in triplicate. The photoproduct of **2** was further analyzed by ESI-MS (Supplementary Figure S8).

Stability test. To test the chemical stability of **2** in acetone, we measured the UV–vis spectrum for 1500 seconds without irradiation of the light and compared the temporal changes in the absorbance at 515 nm with the results from photolysis (Figure 2). Cycle time set as 10 seconds shows that there is no decomposition of **2** for 1500 seconds.

X-ray crystallography. Single crystal of **1**-(OTf) for X-ray diffraction were obtained from solutions using a nylon loop (Hampton Research Co.) on a handmade copper plate at –40 °C and mounted on a goniometer head in an N_2 cryostream at 173 K. Data collections were carried out on an image plate diffractometer equipped with a monochromator using Mo K_α radiation (λ = 0.71073 Å) incident beam. The diffraction data were integrated and scaled using the Rigaku Rapid Auto software package. Pristine single crystal of **2**-$(OTf)_2 \cdot CH_3COCH_3$ was coated with Parabar 10312 (Hampton Research Co.) and mounted on the cryo-loop (MiTeGen LLC). The data collection was carried out using a synchrotron-based X-ray source (λ = 0.70000 Å) produced from a PLS-II 2D bending magnet with a silicon(111) double crystal monochromator and Rayonix MS225HS CCD area detector at 235 K. BL2D-SMDC program[6] was used for one set of data collection at the following conditions: detector distance of 66 mm, 1-axis omega scan with $\Delta\omega$ of 3˚ and the exposure time of 1 sec/frame. HKL3000sm (Ver. 717.6)[7] was used for cell refinement, reduction, and absorption correction. The structures were solved by the intrinsic phasing method using SHELXT-2018/2[8] and refined by full-matrix least-squares on F^2 using SHELXL-2019/3[9]. All non-hydrogen atoms were refined anisotropic and all H atoms were placed in geometrically idealized positions and constrained to ride on their parent atoms with C—H = 0.94 – 0.98 Å with U_{iso}(H) values of 1.2 and 1.5 U_{eq} of the parent

atoms. The O-bound H atoms of the coordinated water molecules of **2**-$(OTf)_2 \cdot CH_3COCH_3$ were assigned based on a difference-Fourier map and were refined with distance restraints of 0.95 Å (using the DFIX and DANG commands), and U_{iso}(H) values of $1.5U_{eq}$ of the oxygen atom. Some SHELXL restrains (DFIX, DANG, ISOR and RIGU) had to be used to correct the geometry of the disordered parts (OTf^-) and the thermal parameters of the corresponding atoms. The crystallographic data for **1**-(OTf) and **2**-$(OTf)_2 \cdot CH_3COCH_3$ are listed in Tables S1 and Tables S2 list the selected bond distances and angles, respectively. Crystal data for **1**-(OTf): $C_{26}H_{33}Cl_2F_6FeN_5O_6S_2$, Triclinic, $P\bar{1}$, $Z = 2$, $a = 10.455(2)$, $b = 13.987(3)$, $c = 14.498(3)$ Å, $b = 76.06(3)°$, $V = 1950.6(8)$ Å^3 , $\mu = 0.700$ mm^{-1} , $\rho_{calcd} = 1.390$ g/cm^3, $R_1 = 0.0420$, $wR_2 = 0.1042$ for 6862 unique reflections, 440 variables. Crystal data for **2**-$(OTf)_2 \cdot CH_3COCH_3$: $C_{27}H_{38}Cl_2F_6FeN_5O_9S_2$, Monoclinic, $P2_1/c$, $Z = 4$, $a = 16.573(3)$, $b = 11.195(2)$, $c = 20.950(4)$ Å, $\beta = 105.62(3)°$, $V = 3743.4(14)$ Å^3, $\mu = 0.705$ mm^{-1}, $\rho_{calcd} = 1.564$ g/cm^3, $R_1 = 0.0691$, $wR_2 = 0.2132$ for 6848 unique reflections, 548 variables. CCDC-2452720 for **1**-(OTf) and 242919 for **2**-$(OTf)_2 \cdot CH_3COCH_3$ contain the supplementary crystallographic data for this paper. These data can be obtained free of charge via www.ccdc.cam.ac.uk/data_request/cif (or from the Cambridge Crystallographic Data Centre, 12, Union Road, Cambridge CB2 1EZ, UK; fax: (+44) 1223-336-033; or deposit@ccdc.cam.ac.uk).

In-situ photocrystallography single crystal diffraction for 2-$(OTf)_2 \cdot CH_3COCH_3$. Measurements were conducted under identical conditions as those used for the pristine single crystal, with UV-vis light irradiation. The parameters for each dataset acquisition were as follows: $\Delta\omega = 5°$, with an exposure time of 1 second per frame, covering 120 frames over 360º rotation, totaling 120 seconds. Data collection initiation and completion were controlled by the CCD detector's trigger in/out signal. Accounting for the CCD preparation time of 5 seconds before and after data collection, the total acquisition time for each dataset was 130 seconds.

The crystal remained continuously exposed to UV-vis light for a total of 6,500 seconds, with each dataset captured every 130 seconds in response to the CCD detector's trigger signal. Under continuous UV-vis light irradiation, a gradual decrease in crystallinity and a reduction in high-angle diffraction intensity were observed. While this resulted in slight data degradation, no significant structural issues were detected. Each dataset from 130 to 6,500 seconds, with file numbers from CCDC-2452920 to 2452969, respectively, contains the supplementary crystallographic data for this paper. These data can be obtained free of charge via www.ccdc.cam.ac.uk/data_request/cif (or from the Cambridge Crystallographic Data Centre, 12, Union Road, Cambridge CB2 1EZ, UK; fax: (+44) 1223-336-033; or deposit@ccdc.cam.ac.uk).

II. Synthesis

1. Preparation of [Fe^{II}(Cl−TBDAP)(CH_3CN)(OTf)](OTf) (1-(OTf)). The Cl−TBDAP (210.7 mg. 0.5 mmol) ligand in $CHCl_3$ (2 mL) was added to the solution of anhydrous $FeCl_2$ (63.3 mg, 0.5 mmol) in CH_3CN (2 mL) and the reaction mixture was stirred overnight under N_2. After the reaction, two equivalents of AgOTf (259.5 mg, 1 mmol) in CH_3CN (1 mL) were added to the reaction mixture and stirred for 30 min. The white solid of AgCl was precipitated and filtered by a disk filter. The yellow powder of **1** was isolated by adding excess Et_2O and dried under vacuum. Obtained complex **1** was redissolved in CH_3CN and crystalized by slow Et_2O diffusion. The greenish-yellow crystal was obtained. Yield: 231.8 mg (56.8%); UV-vis in acetone: λ_{max} (ε) = 387 nm (445 M^{-1} cm^{-1}); ESI-MS (*m/z*) in CH_3CN: [Fe^{II}(Cl−TBDAP)(CH_3CN)]$^{2+}$ calcd. for $C_{24}H_{33}Cl_2FeN_5$, 258.6; found, 258.8, [Fe^{II}(Cl−TBDAP)(CH_3CN)(H_2O)]$^{2+}$ calcd. for $C_{24}H_{35}Cl_2FeN_5O$, 267.6; found, 267.5, [Fe^{II}(Cl−TBDAP)(CH_3CN)$_2$]$^{2+}$ calcd. for $C_{26}H_{36}Cl_2FeN_6$, 279.0; found, 279.1, and [Fe^{II}(Cl−TBDAP)(CH_3CN)$_2$(H_2O)]$^{2+}$ calcd. for $C_{26}H_{38}Cl_2FeN_6O$, 288.1; found, 288.0; analysis

(calcd., found for $C_{24}H_{30}Cl_2F_6FeN_4O_6S_2$): C (37.18, 36.92), H (3.90, 3.85), N (7.23, 6.99). The elemental analysis (EA) result showed that solvent in [Fe^{II}(Cl−TBDAP)(CH_3CN)(OTf)](OTf) may fall off according to previously reported literature[10].

2. Preparation of [Fe(Cl−TBDAP)(NO)(H_2O)](OTf)$_2$·CH_3COCH_3 (2-(OTf)$_2$·CH_3COCH_3). The purified excess NO• gas was added to the solution of precursor **1** (50 mg, 0.06 mmol) in acetone (3 mL) at −20 °C under N_2. The yellow solution of **1** turned to reddish-brown nitrosyl complex **2** upon the addition of NO• gas. The nitrosyl complex **2** was crystalized by Et_2O layering and stored at −40 °C for 2 days. The brown crystals of **2** were obtained and washed by Et_2O three times and dried under vacuum. Yield: 38.8 mg (77.5%); ATR-IR (crystal): 1766 cm^{-1} (ν_{NO}); UV-vis in acetone: λ_{max} (ε) = 408 nm (1027 M^{-1} cm^{-1}), 515 (351 M^{-1} cm^{-1}), and 741 nm (138 M^{-1} cm^{-1}); EPR in acetone at 100 K: g = 3.71, 1.99; effective magnetic moment: 4.26 μ_B; CSI-MS (*m/z*) in acetone: [Fe(Cl−TBDAP)(NO)(CH_3COCH_3)]$^{2+}$ calcd. for $C_{25}H_{36}Cl_2FeN_5O_2$, 282.0; found, 282.1 and [Fe(Cl−TBDAP)(NO)(OTf)]$^+$ calcd. for $C_{23}H_{30}Cl_2F_3FeN_5O_4S$, 655.1; found, 654.9; analysis (calcd., found for $C_{27}H_{38}Cl_2F_6FeN_5O_9S_2$): C (36.79, 36.63), H (4.35, 4.77), N (7.95, 7.99).

III. Computational Studies

1. Computational Details. All molecular structures except for the excited states mentioned below were carried out using DFT[11] as implemented in ORCA 4.2.0.[12]. Geometry optimizations were performed with the B3LYP including Grimme's D3 dispersion correction with Becke-Johnson damping[13–18]. Geometry optimizations and analytical vibrational frequency calculations were carried out with the def2-SVP basis set[19]. For all optimized structures, the intermediates were confirmed with no imaginary vibrational frequency, while transition states showed a single imaginary frequency with a motion corresponding to the proper transitions.

The solvated energies of optimized structures were re-evaluated by additional single-point calculations on each optimized geometry using the def2-TZVP basis set[19]. For all calculations, the RIJCOSX approximation[20–24] was utilized with the auxiliary basis set def2/J[25]. To model the solution environment for acetone, the solvation model based on density (CPCM)[26,27] was utilized with parameters which have been implemented in ORCA. In the results reported, solvation calculations were carried out with the def2-SVP basis at the optimized gas-phase geometry employing the dielectric constants of $\varepsilon = 20.7$ for acetone, respectively. As is the case for all continuum models, the solvation energies are subject to empirical parametrization of the atomic radii that are used to generate the solute surface. We employed the standard set of optimized radii in ORCA for H (1.300 Å), C (2.000 Å), N (1.830 Å), O (1.720 Å), Fe (2.223 Å), Cl (2.050 Å). Analytical vibrational frequencies within the harmonic approximation were computed with the def2-SVP basis to confirm proper convergence to well-defined minima or saddle points on the potential energy surface. The energy components have been computed with the following protocol. The free energy in solution-phase, G(sol), has been calculated as follows:

$$G(sol) = G(gas) + Gsolv$$

$$G(gas) = H(gas) – TS(gas)$$

$$H(gas) = E(SCF) + ZPE$$

$$\Delta E(SCF) = \sum E(SCF) \text{ for products} – \sum E(SCF) \text{ for reactants}$$

$$\Delta G(sol) = \sum G(sol) \text{ for products} – \sum G(sol) \text{ for reactants}$$

2. Complete active space self-consistent field (CASSCF). To make our computations tractable, DFT optimized structures were used for multiconfigurational calculations. For better convergence, active orbitals for multiconfigurational calculations are derived from unrestricted

natural orbitals. All CASSCF results were calculated using def2-TZVP basis on all atoms along with CPCM correction. The choice of the active space is the most critical decision in any CASSCF study. A general series of rules for how to choose appropriate active space for a transition-metal complex has been established elsewhere[28,29] and was generally followed here. Thus, all five d-orbitals and important ligand-based orbitals (e.g. NO-π* orbitals) were included accordingly. Active space conservation of every single calculation was examined for proper convergence. To accelerate CASSCF calculations, we employed resolution of identity (RI) approximation with def2/J and def2-TZVP/C auxiliary basis sets.

3. Excited state calculations. To simulate excited states, state-averaged CASSCF (SA-CASSCF) calculations with 20 roots were computed with the pre-optimized ground state CAS wavefunction. Similar to the ground state calculations, the def2-TZVP basis on all atoms was used along with CPCM correction. With the optimized SA-CAS wavefunction, strongly contracted NEVPT2 (SC-NEVPT2) calculations were carried out accordingly in order to restore the dynamic correlation energy missing in CASSCF results. Electronic absorption spectra were simulated by the perturbed wave function and the simulated spectra were plotted with Gaussian broadening of 1000 cm^{-1} width. The optimized active spaces were projected into natural orbital manifolds and the orbitals were plotted with Chimera software[30].

4. Geometry optimization with CASSCF level of theory. Most quantum software that supports CASSCF calculations provides geometry optimization with numerical frequency calculations. As a result, while calculations for small molecules often converge quickly, those for larger molecules can take a significantly longer time. To accelerate the calculation process, we employed a new software BAGEL[31], which supports analytic frequency calculations during the geometry optimization process. With the same active spaces that we selected from previous

sections, we performed the geometry optimization calculation to the first excited states of ^{4}**2**. As a result, as shown in the graph in the main text, we observed that the Fe complex and NO separate and stabilize. Notably, the calculation terminated before full convergence because a single wavefunction cannot represent the two dissociated molecules. This result is consistent with the prediction that NO will be released through excitation.

IV. Supplementary Figures

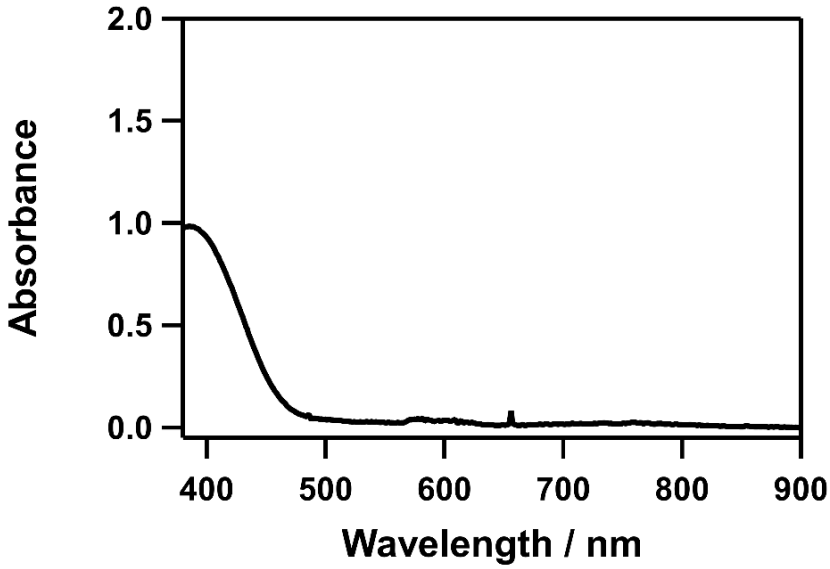

Supplementary Figure S1. UV-vis spectrum of $[Fe^{II}(Cl{-}TBDAP)(CH_3CN)(OTf)]^+$ (**1**) (2 mM) in acetone at −40 °C

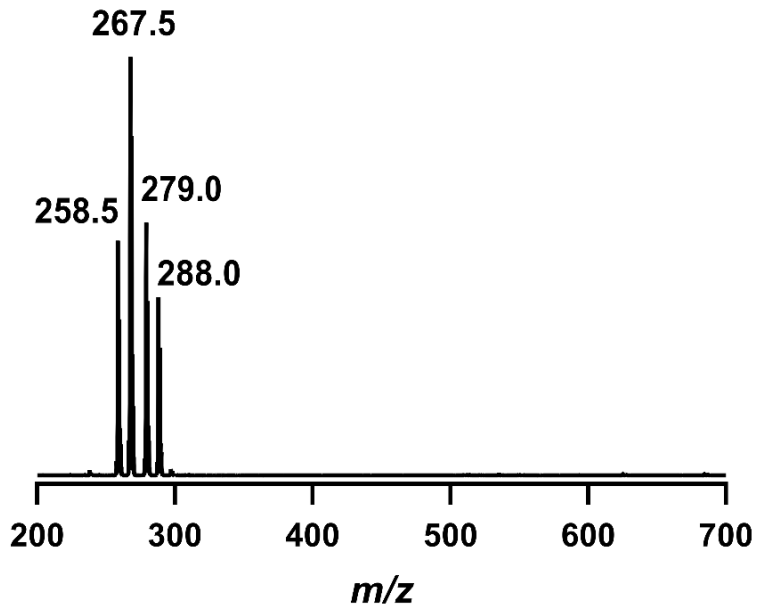

Supplementary Figure S2. ESI-MS spectrum of $[Fe^{II}(Cl{-}TBDAP)(CH_3CN)(OTf)]^+$ (**1**) in CH_3CN. Mass peaks at *m/z* = 258.8, 267.5, 279.0, and 288.0 are assigned to $[Fe^{II}(Cl{-}TBDAP)(CH_3CN)]^{2+}$ (calcd. *m/z* = 258.6), $[Fe^{II}(Cl{-}TBDAP)(CH_3CN)(H_2O)]^{2+}$ (calcd. *m/z* = 267.6), $[Fe^{II}(Cl{-}TBDAP)(CH_3CN)_2]^{2+}$ (calcd. *m/z* = 279.1) and $[Fe^{II}(Cl{-}TBDAP)(CH_3CN)_2(H_2O)]^{2+}$ (calcd. *m/z* = 288.1), respectively.

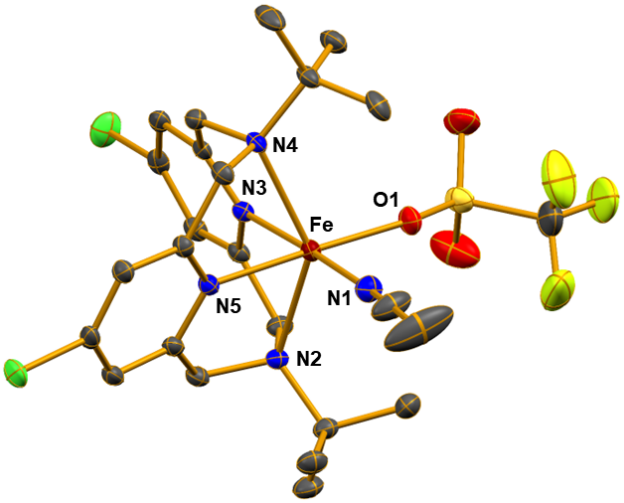

Supplementary Figure S3. ORTEP diagram of $[Fe^{II}(Cl{-}TBDAP)(CH_3CN)(OTf)]^+$ (**1**) with thermal ellipsoids drawn at the 30% probability level. Hydrogen atoms are omitted for clarity. Fe, scarlet; O, red; N, blue; C, dark gray; Cl, green; F, yellowish green; S, yellow.

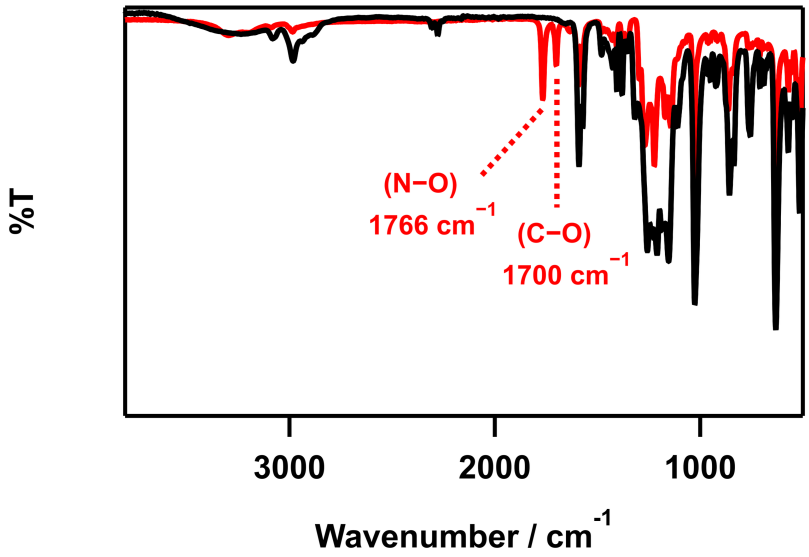

Supplementary Figure S4. The full range of solid state ATR-IR spectra for $[Fe^{II}(Cl{-}TBDAP)(CH_3CN)(OTf)]^+$ (**1**) (black) and $[Fe(Cl{-}TBDAP)(NO)(H_2O)]^{2+}$ (**2**) (red). The vibration energy of N−O in **2** was determined to be 1766 cm^{-1}. The C−O vibration energy of 1700 cm^{-1} originates from an acetone solvent molecule that is co-crystallized within the crystal lattice.

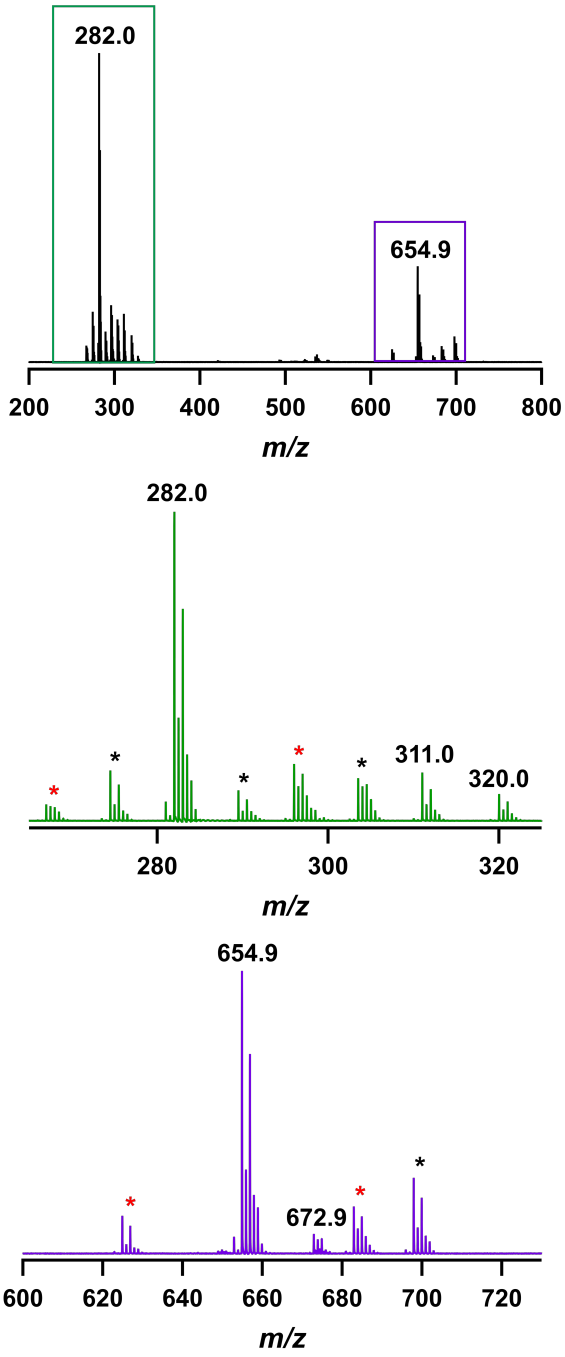

Supplementary Figure S5. CSI-MS spectrum of $[Fe(Cl{-}TBDAP)(NO)(H_2O)]^{2+}$ (**2**) in acetone at −30 °C. Mass peaks at *m/z* = 282.0, 311.0, 320.0, 654.9, and 672.9 are assigned to $[Fe(Cl{-}TBDAP)(NO)(CH_3COCH_3)]^{2+}$ (calcd. *m/z* = 282.1), $[Fe(Cl{-}TBDAP)(NO)(CH_3COCH_3)_2]^{2+}$ (calcd. *m/z* = 311.1), $[Fe(Cl{-}TBDAP)(NO)(H_2O)(CH_3COCH_3)_2]^{2+}$ (calcd. *m/z* = 320.1), $[Fe(Cl{-}TBDAP)(NO)(OTf)]^{+}$ (calcd. *m/z* = 655.1) and $[Fe(Cl{-}TBDAP)(NO)(OTf)(CH_3COCH_3)]^{+}$ (calcd. *m/z* = 673.1), respectively. Asterisk (*) marks are some unidentified species (black) and Fe(II) species (red) due to thermal instability.

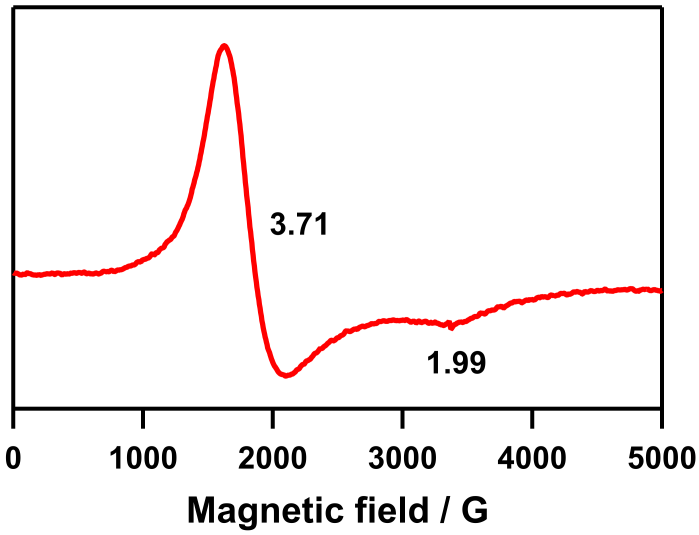

Supplementary Figure S6. X-band EPR spectrum of $[Fe^{II}(Cl{-}TBDAP)(NO)(H_2O)]^{2+}$ (**2**) (8 mM) in frozen acetone at 100 K. Spectroscopic settings: frequency = 9.422 GHz, microwave power = 1.002 mW, modulation frequency = 100 kHz, and modulation amplitude = 5 G.

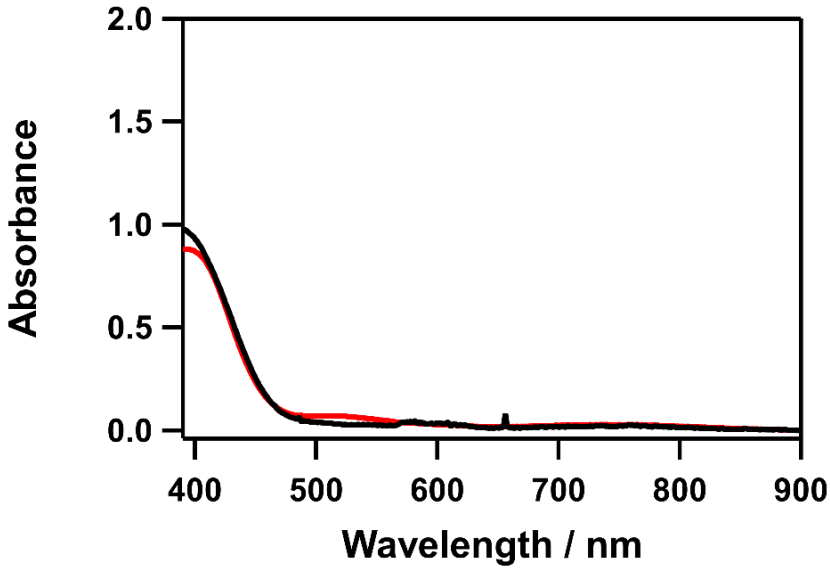

Supplementary Figure S7. Comparison of UV-vis spectrum between $[Fe^{II}(Cl{-}TBDAP)(CH_3CN)(OTf)]^+$ (**1**) (black) and $[Fe(Cl{-}TBDAP)(NO)(H_2O)]^{2+}$ (**2**) (red) after photolysis in acetone at −40 °C.

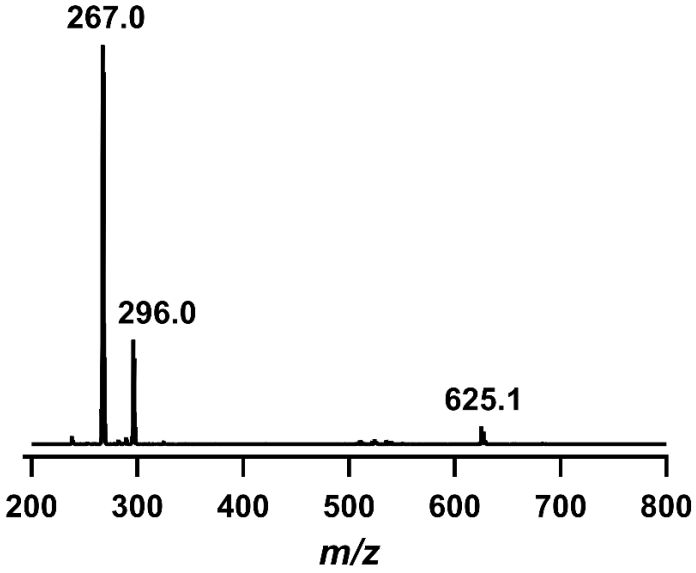

Supplementary Figure S8. ESI-MS spectrum of $[Fe(Cl{-}TBDAP)(NO)(H_2O)]^{2+}$ (**2**) in acetone after photolysis. Mass peaks at *m/z* = 267.0, 296.0 and 625.1 are assigned to $[Fe^{II}(Cl{-}TBDAP)(CH_3COCH_3)]^{2+}$ (calcd. *m/z* = 267.1), $[Fe^{II}(Cl{-}TBDAP)(CH_3COCH_3)_2]^{2+}$ (calcd. *m/z* = 296.1) and $[Fe^{II}(Cl{-}TBDAP)(OTf)]^{+}$ (calcd. *m/z* = 625.1), respectively.

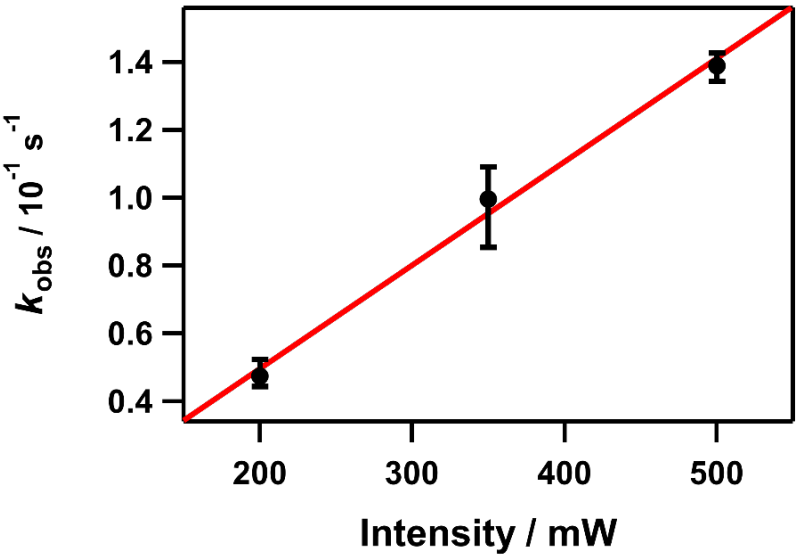

Supplementary Figure S9. Plot of photodissociation rate constants (k_{obs}) of $[Fe(Cl{-}TBDAP)(NO)(H_2O)]^{2+}$ (**2**) against the intensity of xenon lamp.

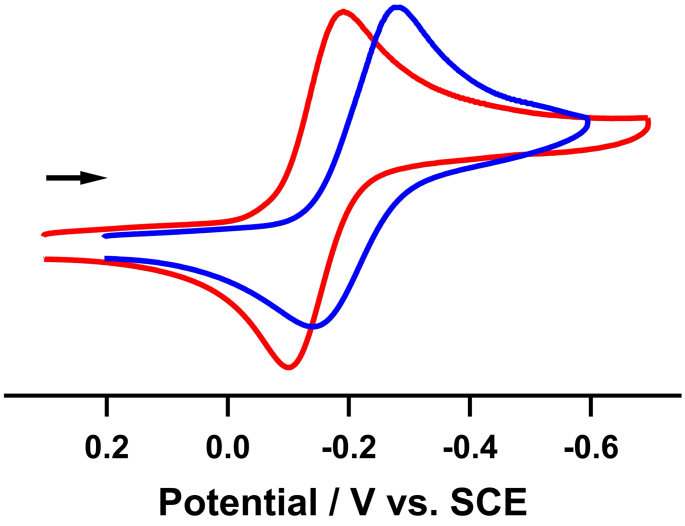

Supplementary Figure S10. Cyclic voltammograms of **2** (red) and $[Fe(TBDAP)(NO)(H_2O)]^{2+}$ (blue) in acetone (1 mM) containing 0.1 M Bu_4NPF_6 at −50 °C (working electrode, Pt; counter electrode, Pt; reference electrode, Ag/Ag^+; scan rate = 200 mV s^{-1}). Redox potential ($E_{1/2}$) of **2** and $[Fe(TBDAP)(NO)(H_2O)]^{2+}$ are determined to be −0.15 and −0.21 V, respectively. A higher redox potential of **2** was achieved by substitution of the H group with an electron-withdrawing Cl group, resulting in an electron-deficient environment for the Fe center.

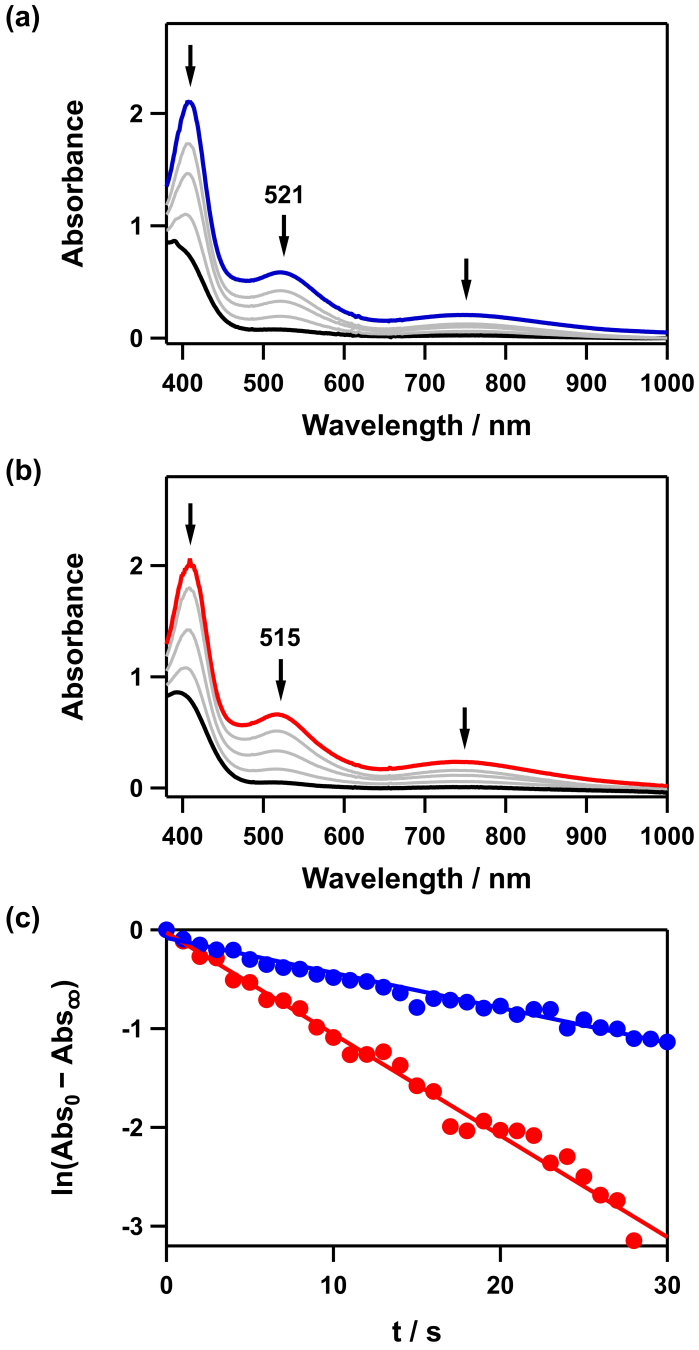

Supplementary Figure S11. UV-vis spectral changes observed in the photolysis reaction of (a) $[Fe(TBDAP)(NO)(H_2O)]^{2+}$ and (b) $[Fe(Cl{-}TBDAP)(NO)(H_2O)]^{2+}$ (**2**) in acetone at −40 °C under white light (λ_{irr} = 385-740 nm, 500 mW, xenon lamp). (c) First-order plots of $[Fe(TBDAP)(NO)(H_2O)]^{2+}$ (bule) and **2** (red). Rate constants (k_{obs}) of $[Fe(TBDAP)(NO)(H_2O)]^{2+}$ and **2** were determined to be 3.37×10^{-2} s^{-1} and 1.06×10^{-1} s^{-1}, respectively.

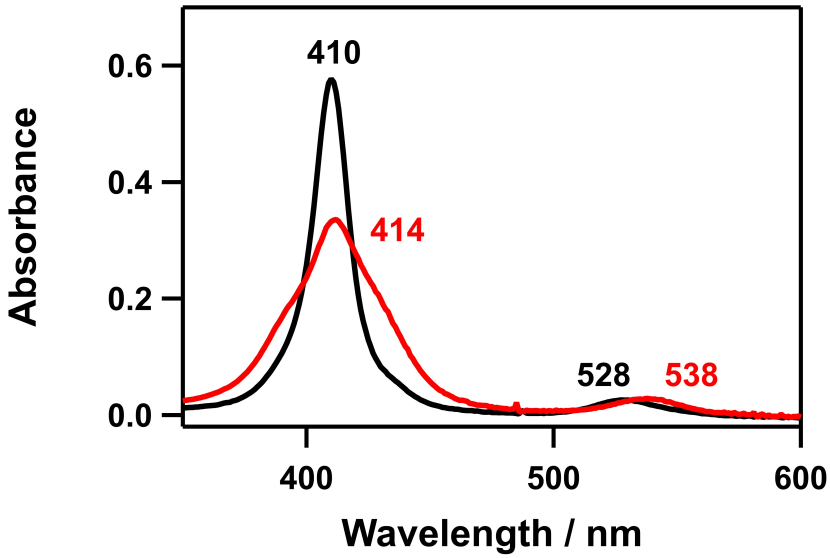

Supplementary Figure S12. Spectral evidence for NO• transfer from $[Fe(Cl{-}TBDAP)(NO)(H_2O)]^{2+}$ (**2**) in acetone to [Co(TPP)] in CH_2Cl_2. Electronic absorption spectra of [Co(TPP)] (black) shift to [Co(NO)(TPP)] (red) after 30 min photoirradiation[32]. The detection of NO• was performed in an H-shaped Schlenk tube.

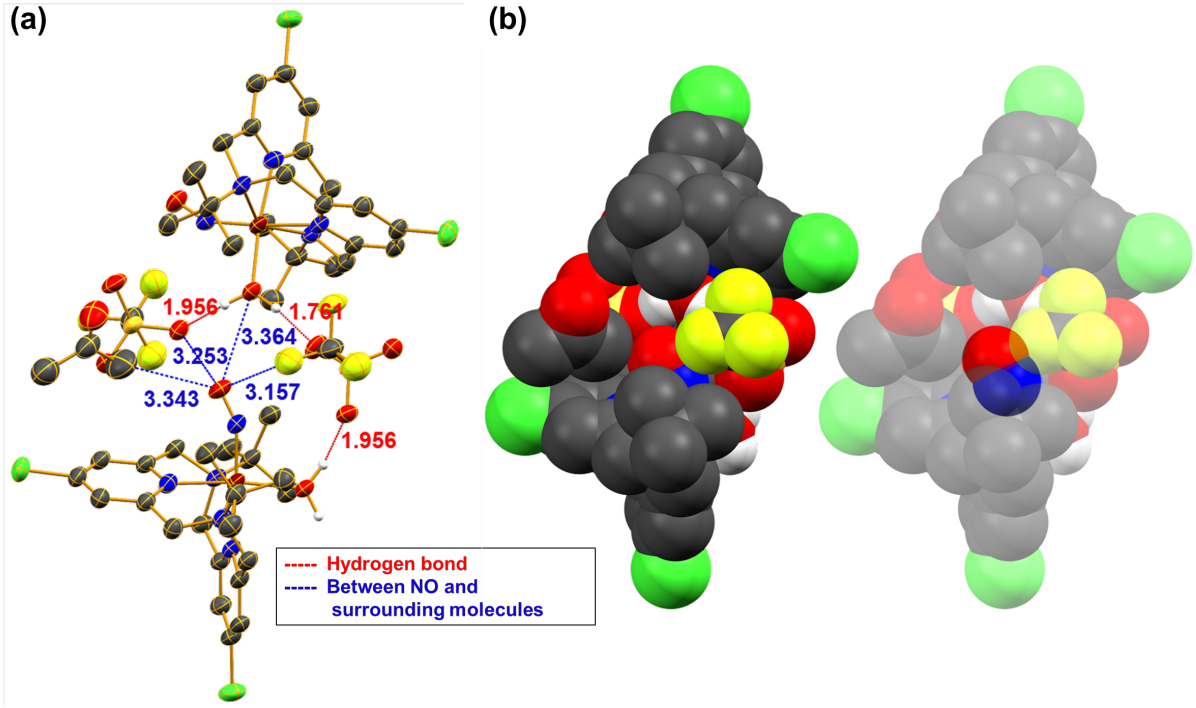

Supplementary Figure S13. Structural encumbrance around the NO moiety. ORTEP diagram with thermal ellipsoids drawn at the 30% probability level. Hydrogen atoms are omitted for clarity except for water. Fe, scarlet; O, red; N, blue; C, dark gray; Cl, green; F, yellowish green; S, yellow. (a) The hydrogen bonding interactions between triflate (OTf^-) and the H_2O ligand are represented (red dotted line). The distances between surrounding molecules and the NO ligand are illustrated (blue dotted line). (b) A space-filling representation around the NO ligand (left) and transparent depiction (right).

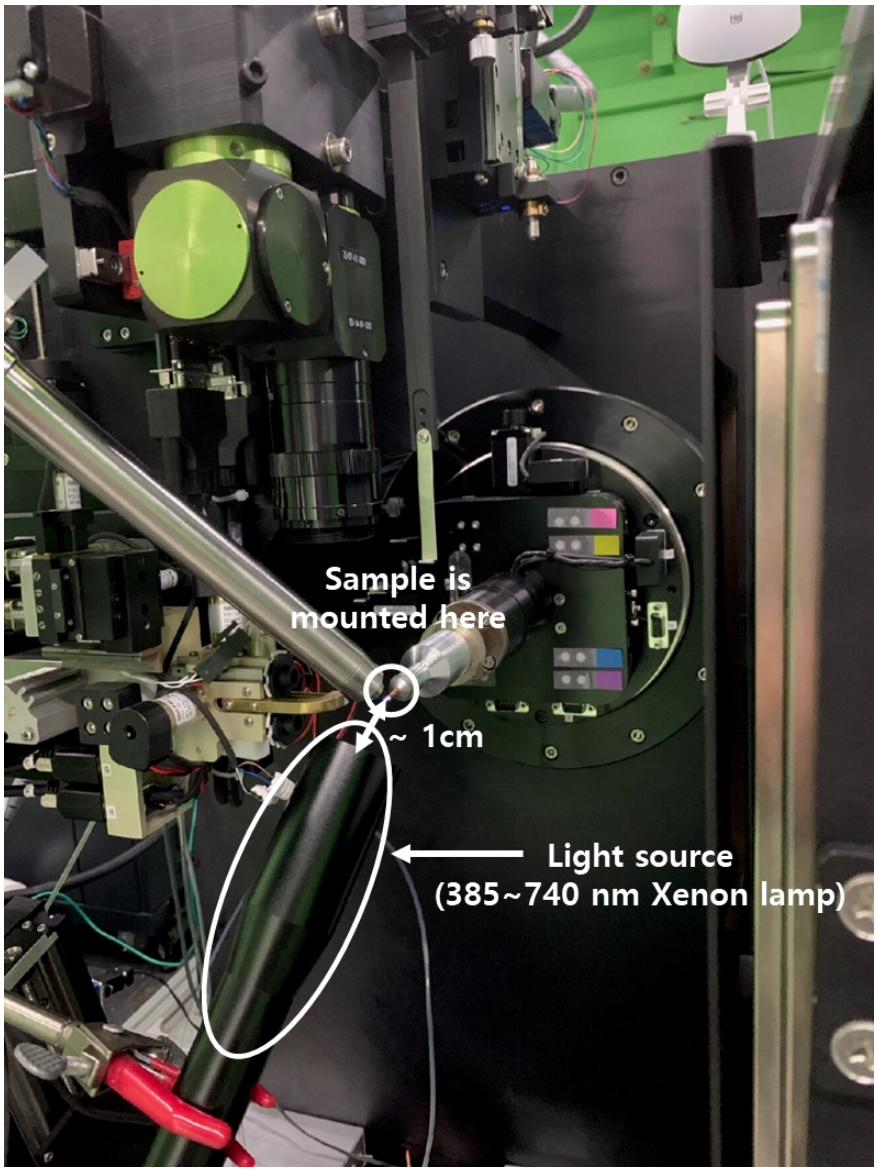

Supplementary Figure S14. Instrumental setup for synchronous in-situ single crystal photocrystallogaphy. The xenon lamp was positioned ~1 cm beneath the goniohead of default equipment for diffraction in the beamline. Before turning on the light, the single crystal of **2** was mounted on the goniohead, then the X-ray structure of pristine was obtained. After measurement of the pristine structure, serial data collections every 130 seconds of the diffraction pattern of samples were carried out under continuous irradiation from a xenon lamp.

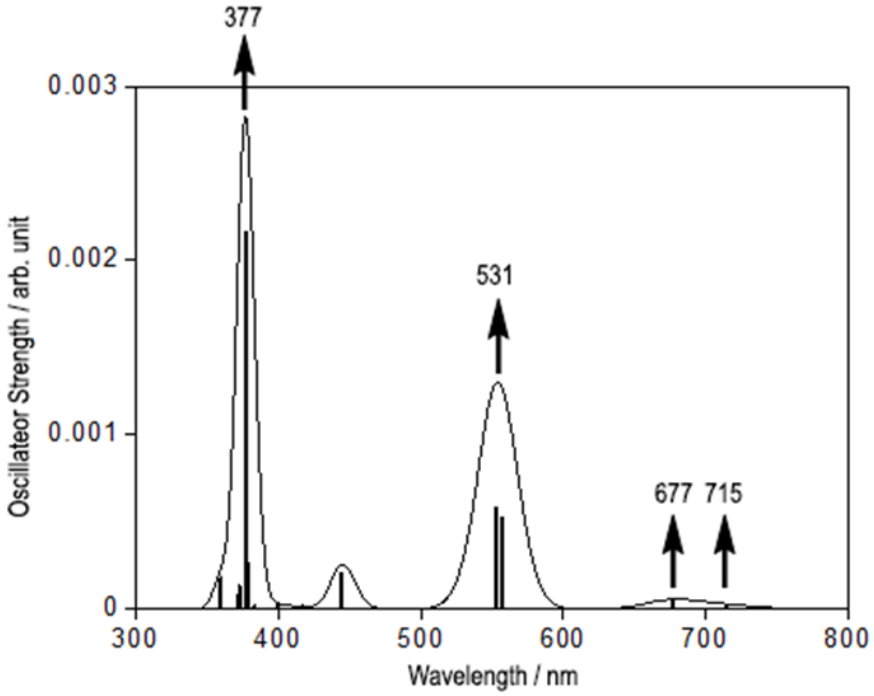

Supplementary Figure S15. NEVPT2/SA-CASSCF(11,9)/def2-TZVP-computed absorption spectrum of **2**.

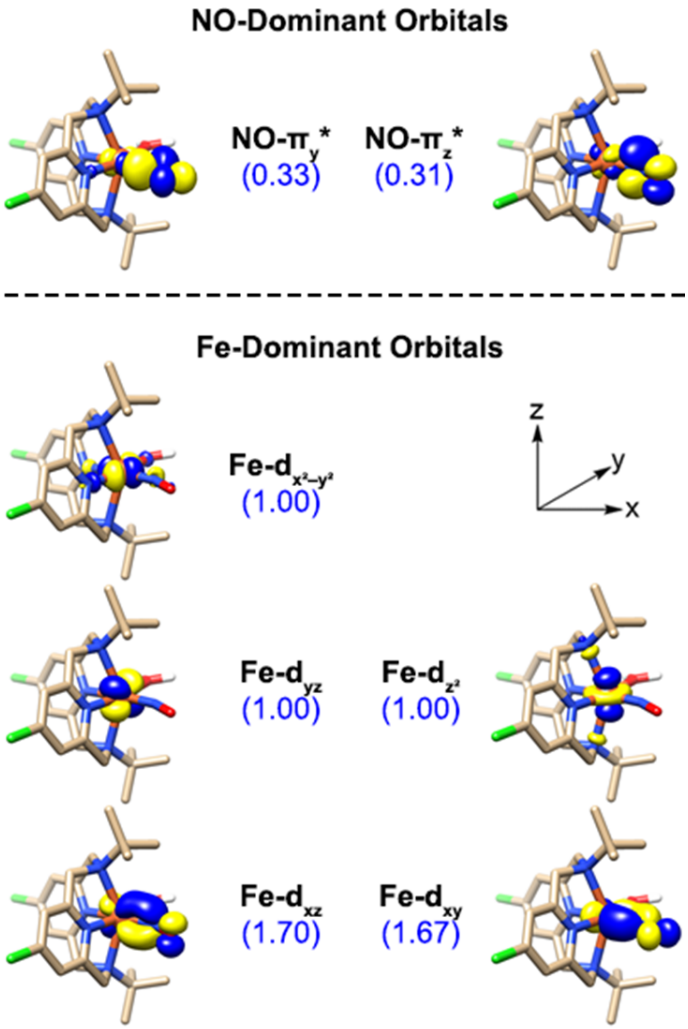

Supplementary Figure S16. NEVPT2/CASSCF(11,9)-computed configurations of 42 projected into natural orbital manifolds. Hydrogen atoms are omitted for clarity and isovalue of 0.05 a.u. is used. The identical electron density represented in Fig. 4 were projected to the natural orbital for analyzing the bonding nature of Fe–NO complex.

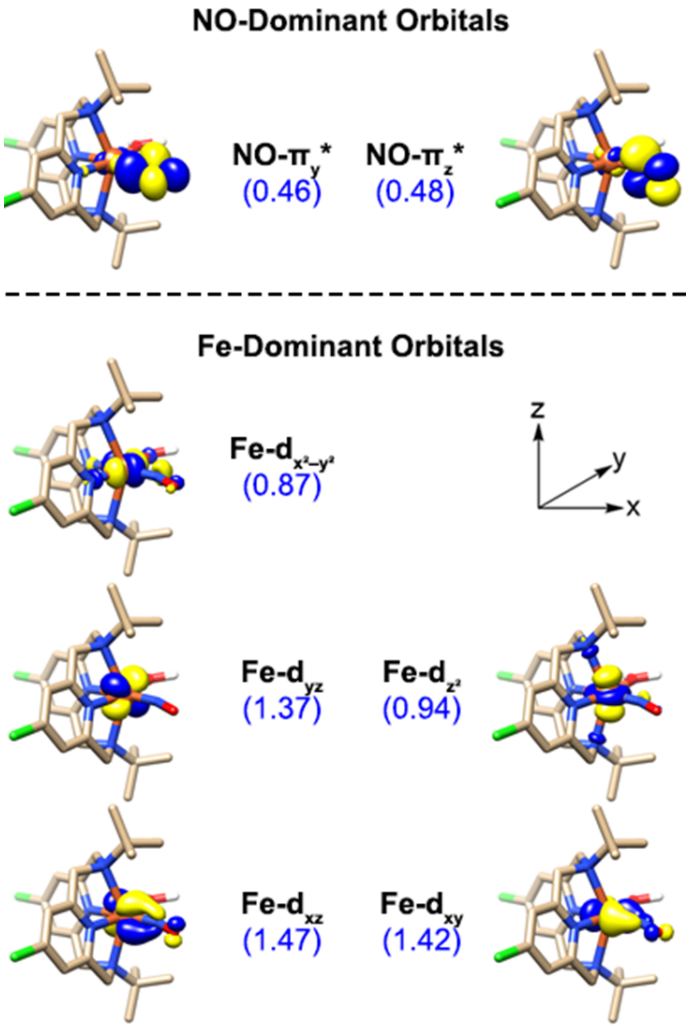

Supplementary Figure S17. NEVPT2/SA-CASSCF(11,9)-computed configurations of 42 with 20 excited states projected into natural orbital manifolds. Hydrogen atoms are omitted for clarity and isovalue of 0.05 a.u. is used. Compared to electron density represented from Supplementary Figure S17, the electron density on the Fe-dominant orbital moved to the NO-dominant orbital, while considering the excited state. This implies that through these transitions, the electron density moved from the Fe–NO bonding orbitals to Fe–NO antibonding orbitals.

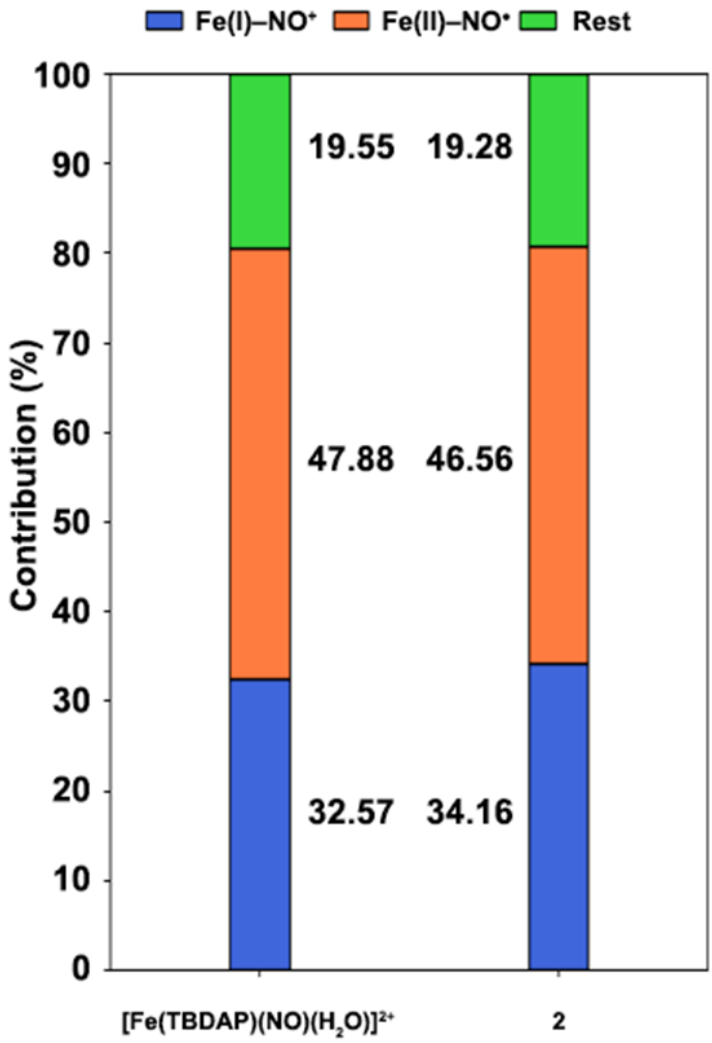

Supplementary Figure S18. The bar graphs highlight the Fe^{I}–NO^{+} configuration percentage of $[Fe(TBDAP)(NO)(H_2O)]^{2+}$ and **2** involved in reaching the MLCT state. The percentage of Fe^{I}–NO^{+} configuration in **2** is raised by the electron-withdrawing Cl group.

V. Supplementary Tables

Supplementary Table S1. Crystal data and structural refinements for **1**-(OTf) and **2**-$(OTf)_2 \cdot CH_3COCH_3$

	1-(OTf)	**2**-$(OTf)_2 \cdot CH_3COCH_3$
Empirical formula	$C_{26}H_{33}Cl_2F_6FeN_5O_6S_2$	$C_{27}H_{38}Cl_2F_6FeN_5O_9S_2$
Formula weight	816.44	881.49
Temperature / K	173(2)	235(2)
Wavelength / Å	0.71073	0.700
Crystal system/space group	Triclinic, $P\bar{1}$	Monoclinic, $P2_1/c$
Unit cell dimensions		
a / Å	10.455(2)	16.573(3)
b / Å	13.987(3)	11.195(2)
c / Å	14.498(3)	20.950(4)
α / °	87.76	90
β / °	76.06(3)	105.62(3)
γ / °	71.57(3)	90
Volume / Å^3	1950.6(8)	3743.4(14)
Z	2	4
Calculated density / g cm^{-3}	1.390	1.564
Absorption coefficient / mm^{-1}	0.700	0.705
Reflections collected	15359	25081
Independent reflections [R(int)]	6862 [0.0147]	6848 [0.0729]
Refinement method	Full-matrix least-squares on F^2	Full-matrix least-squares on F^2
Data/restraints/parameters	6862 / 0 / 440	6848 / 408 / 548
Goodness-of-fit on F^2	1.025	1.099
Final R indices [I > 2sigma(I)]	R_1 = 0.0420, wR_2 = 0.1042	R_1 = 0.0691, wR_2 = 0.2132
R indices (all data)	R_1 = 0.0480, wR_2 = 0.1080	R_1 = 0.0922, wR_2 = 0.2285

Supplementary Table S2. Selected bond distances (Å) and angles (º) for **1**-(OTf) and **2**-$(OTf)_2 \cdot CH_3COCH_3$

Bond distances / Å			
1-(OTf)		**2**-$(OTf)_2 \cdot CH_3COCH_3$	
Fe−N1	2.125(2)	Fe−N1	1.762(4)
Fe−N2	2.390(2)	Fe−N2	2.307(4)
Fe−N3	2.087(2)	Fe−N3	2.067(4)
Fe−N4	2.357(2)	Fe−N4	2.309(4)
Fe−N5	2.109(2)	Fe−N5	2.043(4)
Fe−O1	2.0602(19)	Fe−O2	2.062(3)
		N1−O1	1.157(4)

Bond angles / °			
1-(OTf)		**2**-$(OTf)_2 \cdot CH_3COCH_3$	
N1−Fe−N2	106.80(9)	N1−Fe−N2	97.57(16)
N1−Fe−N3	173.43(9)	N1−Fe−N3	175.28(15)
N1−Fe−N4	98.11(9)	N1−Fe−N4	107.44(16)
N1−Fe−N5	90.02(9)	N1−Fe−N5	91.83(16)
N1−Fe−O1	90.86(9)	N1−Fe−O2	94.99(15)
N2−Fe−N3	74.46(8)	N2−Fe−N3	78.33(14)
N2−Fe−N4	140.48(7)	N2−Fe−N4	144.23(14)
N2−Fe−N5	76.06(8)	N2−Fe−N5	74.75(14)
N2−Fe−O1	101.51(8)	N2−Fe−O2	104.82(13)
N3−Fe−N4	77.61(8)	N3−Fe−N4	75.29(14)
N3−Fe−N5	84.01(8)	N3−Fe−N5	84.87(14)
N3−Fe−O1	95.21(8)	N3−Fe−O2	88.36(13)
N4−Fe−N5	73.72(8)	N4−Fe−N5	79.19(14)
N4−Fe−O1	108.39(8)	N4−Fe−O2	98.18(13)
N5−Fe−O1	177.57(8)	N5−Fe−O2	173.16(14)
		Fe−N1−O2	152.8(4)

Supplementary Table S3. Bond distance (Å) and angle (°) changes of **2**-$(OTf)_2 \cdot CH_3COCH_3$ against exposure time of visible light (λ_{irr} = 385–740 nm).

Time (s)	Fe−N1 (Å)	N1−O1 (Å)	Fe−N1−O1 (°)
Pristine	1.762(4)	1.157(4)	152.8(4)
130	1.762(4)	1.156(4)	152.3(4)
260	1.763(4)	1.156(5)	152.6(4)
390	1.764(4)	1.151(5)	152.5(4)
520	1.766(4)	1.152(5)	152.7(4)
650	1.769(4)	1.148(5)	152.5(4)
780	1.772(4)	1.146(5)	152.4(4)
910	1.771(4)	1.145(5)	152.6(4)
1040	1.772(4)	1.147(5)	152.2(4)
1170	1.775(4)	1.140(5)	152.4(4)
1300	1.777(4)	1.136(5)	151.8(4)
1430	1.779(4)	1.137(5)	152.2(4)
1560	1.784(4)	1.132(5)	152.1(4)
1690	1.782(5)	1.136(5)	152.0(4)
1820	1.780(5)	1.133(5)	152.0(5)
1950	1.783(5)	1.127(5)	152.3(5)
2080	1.786(5)	1.128(5)	152.1(5)
2210	1.782(5)	1.132(5)	151.8(5)
2340	1.789(5)	1.126(6)	151.6(5)
2470	1.784(5)	1.126(6)	151.9(5)
2600	1.792(5)	1.117(6)	152.0(5)
2730	1.792(5)	1.121(6)	151.7(5)
2860	1.793(5)	1.118(6)	151.9(5)
2990	1.796(6)	1.119(6)	150.9(5)
3120	1.795(6)	1.119(6)	151.0(6)
3250	1.796(6)	1.110(6)	151.5(6)

Time (s)	Fe−N1 (Å)	N1−O1 (Å)	Fe−N1−O1 (°)
3380	1.798(6)	1.110(6)	151.6(6)
3510	1.794(6)	1.115(6)	150.8(6)
3640	1.802(6)	1.115(6)	150.9(6)
3770	1.801(6)	1.113(7)	150.4(6)
3900	1.796(7)	1.113(7)	150.8(6)
4030	1.800(7)	1.113(7)	151.1(6)
4160	1.792(7)	1.115(7)	151.1(7)
4290	1.799(7)	1.110(7)	151.1(7)
4420	1.800(7)	1.110(7)	151.5(7)
4550	1.798(7)	1.110(7)	150.9(7)
4680	1.792(7)	1.112(7)	151.8(7)
4810	1.805(7)	1.104(7)	151.2(7)
4940	1.801(8)	1.110(7)	151.0(7)
5070	1.810(8)	1.106(7)	150.3(7)
5200	1.800(8)	1.110(8)	151.5(8)
5330	1.801(8)	1.103(8)	151.7(8)
5460	1.802(9)	1.102(8)	151.2(8)
5590	1.806(9)	1.109(8)	151.1(8)
5720	1.803(9)	1.104(8)	151.2(8)
5850	1.802(9)	1.117(8)	150.1(9)
5980	1.801(9)	1.104(8)	150.6(9)
6110	1.803(9)	1.104(8)	151.2(9)
6240	1.793(9)	1.107(8)	151.5(9)
6370	1.808(10)	1.107(9)	150.1(10)
6500	1.805(10)	1.103(9)	150.9(10)

Supplementary Table S4. Experimentally determined bond lengths (in Å) and angles (in Degrees) for **2** along with calculated values.

	Exp.	^{2}**2** (Calc.)	^{4}**2** (Calc.)	^{6}**2** (Calc.)
Fe–NO (Å)	1.762(4)	1.775	1.785	2.099
N–O (Å)	1.157(4)	1.161	1.154	1.153
Fe–N–O (°)	152.8(4)	145.22	163.84	155.38
ΔG(sol) (kcal/mol)	–		0.00	13.89

Supplementary Table S5. CASSCF(11,9)-computed configurations of **^{4}2** projected into a Foster-Boys localized orbital.

	Electronic configuration	**Weight**
$\|^4\Phi_1\rangle$	$\|(\text{Fe-d}_{x^2-y^2})^{\uparrow}(\text{Fe-d}_{xy})^{\uparrow}(\text{Fe-d}_{z^2})^{\uparrow}(\text{Fe-d}_{yz})^{\uparrow}(\text{Fe-d}_{xz})^{\uparrow}(\text{NO-}\pi^*_y)^{\downarrow}(\text{NO-}\pi^*_z)^{\downarrow}\rangle$	44.6
$\|^4\Phi_2\rangle$	$\|(\text{Fe-d}_{x^2-y^2})^{\uparrow}(\text{Fe-d}_{xy})^{\uparrow}(\text{Fe-d}_{z^2})^{\uparrow}(\text{Fe-d}_{yz})^{\uparrow}(\text{Fe-d}_{xz})^{\uparrow\downarrow}(\text{NO-}\pi^*_y)^{\downarrow}(\text{NO-}\pi^*_z)^{0}\rangle$	15.3
$\|^4\Phi_3\rangle$	$\|(\text{Fe-d}_{x^2-y^2})^{\uparrow}(\text{Fe-d}_{xy})^{\uparrow\downarrow}(\text{Fe-d}_{z^2})^{\uparrow}(\text{Fe-d}_{yz})^{\uparrow}(\text{Fe-d}_{xz})^{\uparrow}(\text{NO-}\pi^*_y)^{0}(\text{NO-}\pi^*_z)^{\downarrow}\rangle$	12.9

Supplementary Table S6. NEVPT2/SA-CASSCF(11,9)-computed configurations of ^{4}**2** projected into natural orbital manifolds. Most important excited states are enumerated. Configurations more than 15% are given below.

State	Excitation Energy (eV / nm)	Oscillator Strength (arb. unit)	Weight	Electronic configuration	Character
Q_0			34.16	$(d_{xz})^2(d_{xy})^2(d_{yz})^1(d_{z^2})^1(d_{x^2-y^2})^1(\pi^*_y)^0(\pi^*_z)^0$	Fe(I)–NO^+
			23.46	$(d_{xz})^2(d_{xy})^1(d_{yz})^1(d_{z^2})^1(d_{x^2-y^2})^1(\pi^*_y)^1(\pi^*_z)^0$	Fe(II)–$NO^\bullet$
			23.10	$(d_{xz})^1(d_{xy})^2(d_{yz})^1(d_{z^2})^1(d_{x^2-y^2})^1(\pi^*_y)^0(\pi^*_z)^1$	Fe(II)–$NO^\bullet$
Q_1	1.734 / 715	1.799×10^{-5}	48.24	$(d_{xz})^1(d_{xy})^1(d_{yz})^2(d_{z^2})^1(d_{x^2-y^2})^1(\pi^*_y)^0(\pi^*_z)^1$	Fe(II)–$NO^\bullet$
			25.52	$(d_{xz})^2(d_{xy})^1(d_{yz})^2(d_{z^2})^1(d_{x^2-y^2})^1(\pi^*_y)^0(\pi^*_z)^0$	Fe(I)–NO^+
Q_2	1.832 / 677	4.811×10^{-5}	51.16	$(d_{xz})^1(d_{xy})^1(d_{yz})^2(d_{z^2})^1(d_{x^2-y^2})^1(\pi^*_y)^1(\pi^*_z)^0$	Fe(II)–$NO^\bullet$
			22.28	$(d_{xz})^1(d_{xy})^2(d_{yz})^2(d_{z^2})^1(d_{x^2-y^2})^1(\pi^*_y)^0(\pi^*_z)^0$	Fe(I)–NO^+
Q_8	2.229 / 556	5.234×10^{-4}	34.19	$(d_{xz})^2(d_{xy})^2(d_{yz})^1(d_{z^2})^1(d_{x^2-y^2})^0(\pi^*_y)^1(\pi^*_z)^0$	Fe(II)–$NO^\bullet$
			28.50	$(d_{xz})^2(d_{xy})^2(d_{yz})^1(d_{z^2})^1(d_{x^2-y^2})^0(\pi^*_y)^0(\pi^*_z)^1$	
Q_9	2.244 / 553	5.755×10^{-4}	34.93	$(d_{xz})^2(d_{xy})^2(d_{yz})^1(d_{z^2})^1(d_{x^2-y^2})^0(\pi^*_y)^0(\pi^*_z)^1$	Fe(II)–$NO^\bullet$
			29.31	$(d_{xz})^2(d_{xy})^2(d_{yz})^1(d_{z^2})^1(d_{x^2-y^2})^0(\pi^*_y)^1(\pi^*_z)^0$	
Q_{10}	3.290 / 377	2.160×10^{-3}	53.61	$(d_{xz})^1(d_{xy})^1(d_{yz})^1(d_{z^2})^1(d_{x^2-y^2})^2(\pi^*_y)^0(\pi^*_z)^1$	Fe(II)–$NO^\bullet$
			17.02	$(d_{xz})^2(d_{xy})^1(d_{yz})^1(d_{z^2})^1(d_{x^2-y^2})^2(\pi^*_y)^0(\pi^*_z)^0$	Fe(I)–NO^+

Supplementary Table S7. Computed energy components of the DFT-optimized structures.

	E(SCF)/(eV) def2-TZVP	**ZPE/(kcal/mol)** def2-SVP	**S(gas)/(cal/mol·K)** def2-SVP	**G(solv)/(kcal/mol)** def2-SVP
^{2}**2**	–94292.140	333.56	188.43	–138.09
^{4}**2**	–94292.468	330.24	195.74	–139.32
^{6}**2**	–94291.721	329.05	202.08	–139.32

Supplementary Table S8. Cartesian coordinates of the optimized geometries.

^{2}2			
Fe	9.52514470024760	6.10019733789915	14.71121804321842
Cl	5.33746108831249	1.67226926865030	16.76270299415375
Cl	5.14313547734797	10.45169500927857	13.20842826484311
O	11.01756763859266	8.37242127658472	14.00857662583086
O	11.08070560488665	4.51577995212550	15.02009884112358
H	11.28493938752951	4.15405788517167	15.89573381915987
H	11.93521354543343	4.68239824631222	14.59166448678459
N	10.78118421741110	7.25638427552768	14.22451734290385
N	9.10914805635423	6.94228081131660	16.73911852148537
N	8.20045638502264	4.76965316848922	15.34093286462522
N	8.88492658181512	5.17690585939174	12.80429610705166
N	8.14108805214031	7.35526276727345	14.30494747273902
C	10.20596394141211	6.81192814361965	17.81758071767119
C	11.56780573712638	7.18840724712345	17.22545939818074
H	12.32753184767721	7.13175478925998	18.01793245320741
H	11.59749365664554	8.21305807969931	16.83031730453632
H	11.86477530332766	6.49435208270553	16.42932719120209
C	9.90521865066638	7.72672153051025	19.01481822429484
H	8.89613922659787	7.57353201556618	19.42843811323255
H	10.02502932721904	8.79070906222468	18.76486140187627
H	10.61598173593201	7.50534465829874	19.82375549341759
C	10.26606962198949	5.35063280504164	18.28886409779818
H	11.17632942261539	5.20045788450805	18.88630736060692
H	10.29090428971099	4.65063392865270	17.44226830386630
H	9.42107052901424	5.06373031586508	18.92843954995055
C	7.82740569703311	6.28616893248504	17.17026512602574
H	6.98778825899504	6.93101462141007	16.86778043433004
H	7.76274367080734	6.21991585842752	18.26354974886242
C	7.58567051208501	4.94706984721619	16.52136857551648
C	6.69546474746016	3.99551865620762	17.00640762362992
H	6.19351065675103	4.12349013611638	17.96637237217773
C	6.43047729735772	2.86909545059846	16.21065030303797
C	7.03687728894606	2.73451883853773	14.94905595926432
H	6.79286674766367	1.88462369770731	14.30991649721519
C	7.93271848034460	3.71805406867951	14.54550916043533
C	8.64810816552677	3.75568525366044	13.21586860429871
H	8.06662584583748	3.20724029850157	12.46061801254588
H	9.62189440530310	3.26006995358748	13.31595736842230
C	9.82105268427401	5.28508951322275	11.57480096389614
C	11.25443142034441	4.90511900960571	11.96428993041302
H	11.87283158530679	4.90080170467927	11.05646274396490
H	11.32572112712160	3.89962778397419	12.40219702238487
H	11.69970695416944	5.64000196971538	12.64972540453723
C	9.35058159730752	4.34542036770954	10.45179249690383
H	8.29442211673094	4.49619022308001	10.18024301623340

H	9.50050030144636	3.28490184028774	10.70158347598102
H	9.94307131011003	4.54820654397831	9.54853157323481
C	9.81716102182979	6.73251819555585	11.06359224522595
H	10.03307235369443	7.46189054906557	11.85282885753019
H	8.87238970937369	7.01526350187331	10.58030003046926
H	10.60030065535918	6.84007888067023	10.29985729671781
C	7.55373759483765	5.82369170660687	12.53825689927655
H	6.76347296562647	5.18235813021610	12.95952584250268
H	7.34131049515374	5.88004716736379	11.46376205752218
C	7.39424486004205	7.16872104850740	13.20124261037912
C	6.45358809408491	8.12023864300151	12.82364986803704
H	5.84947554419389	7.99029604955264	11.92476138999137
C	6.27993763849374	9.24864872769721	13.64186765333420
C	7.01575717285201	9.37926710709685	14.83271075209538
H	6.84056574352705	10.22592232476324	15.49777860348207
C	7.95587041556983	8.40255883596169	15.13401720500915
C	8.80695474977633	8.36432790077085	16.38401494251362
H	9.75131788318254	8.89705303139826	16.20725533882403
H	8.29120420645105	8.88665122941336	17.20384000001573

==========

^{4}2

==========

Fe	9.74482359230700	6.10007189126170	14.68356937783164
Cl	5.31561031798280	1.73629308181564	16.72566109106372
Cl	4.93953347688592	10.29276866605842	13.33569266601907
O	11.55445992548306	8.27240514442603	13.99020828100262
O	11.11297970404659	4.44884371947547	15.15565000577402
H	10.87456557143221	3.65587445747864	15.66059001604703
H	12.07467668475686	4.42197653659996	15.02507329385801
N	10.99255161065130	7.29389418589395	14.23173975389916
N	9.13649013196523	6.98104249175064	16.75569298536118
N	8.28960352738139	4.74746473634940	15.34302723126319
N	8.87988816144320	5.16377100132638	12.74666153315619
N	8.16278932816669	7.37599184256315	14.26926822432148
C	10.20637339078168	6.88847082211287	17.86508159028796
C	11.57530655289315	7.30370388975891	17.31354839192474
H	12.30668221773280	7.28680364518543	18.13401193172892
H	11.58753351497453	8.32162316665485	16.89990949458119
H	11.93430265442688	6.60312028538139	16.54709910000164
C	9.84046625171922	7.79261908917827	19.05209548574354
H	8.83105606378571	7.59046498008906	19.44259232315439
H	9.91044356054597	8.86058494388687	18.79891171134659
H	10.54296470534342	7.61064282690903	19.87797016118075
C	10.31233517765300	5.43015800174212	18.33886237316363
H	11.15443325556428	5.34380653534582	19.04031802807126
H	10.51284384244097	4.75171560251970	17.50073741651656
H	9.42112667513814	5.07585800470640	18.87305362011094
C	7.87095996868949	6.29967442078603	17.15233622714453

H	7.02021690460279	6.92000036045153	16.82831517759125
H	7.77265582153057	6.23092635809094	18.24333083708843
C	7.65366555973331	4.95151391199222	16.50480715843994
C	6.72577601281101	4.02783299397592	16.97860132798430
H	6.20962545825215	4.17620394640923	17.92823370805492
C	6.43960889941894	2.90829661010101	16.18272894424755
C	7.04339999199972	2.76616062205376	14.91996488121403
H	6.76661934516375	1.93577202201096	14.26848407163971
C	7.97506517220806	3.72211925561052	14.53143678085818
C	8.66087202799045	3.75416886932080	13.18154792729639
H	8.06079469664265	3.18730889732789	12.45323510020763
H	9.63835877693835	3.25951504345684	13.24912905555857
C	9.79462785464169	5.27486904241681	11.51069432083821
C	11.21663987236698	4.82027222529754	11.86920653542889
H	11.85161762424492	4.91951939158756	10.97806148690770
H	11.26703549206565	3.76551074878355	12.17570136465898
H	11.66649453131620	5.44444652533835	12.65373811157325
C	9.27640373216157	4.40383211168464	10.35419538686564
H	8.23859483191375	4.63907871606194	10.07412525948343
H	9.34221480085619	3.32846552533214	10.57654746088568
H	9.89471610034978	4.58494693888571	9.46348731041604
C	9.84081921823514	6.74372829428643	11.06344712673913
H	10.12401710351477	7.42271267803848	11.87766766445218
H	8.88852333594506	7.09207792745549	10.64162655018153
H	10.59205971628320	6.85428292171563	10.26881491341716
C	7.55479460469908	5.81447094640016	12.52011347193359
H	6.76697071210500	5.16490307698121	12.93438278739217
H	7.32222628289285	5.89582796437903	11.45056642575997
C	7.38175989266937	7.15087539244701	13.20586511841152
C	6.36973354193891	8.04814879012214	12.87239761474366
H	5.73038356640654	7.88551914833976	12.00333602625326
C	6.16675820026860	9.15807445394496	13.70668281137747
C	6.94427001289041	9.32291955140145	14.86835282892294
H	6.74436498610226	10.14945180168800	15.55173830409746
C	7.94851516182652	8.39572157075556	15.11864282893275
C	8.82092603326155	8.38586458691292	16.35878604790971
H	9.76135490583191	8.91997869026486	16.16002024055898
H	8.30883535372812	8.93296411942042	17.16543771712277

==========

^{6}2

==========

Fe	9.70990704226600	6.02232730948592	14.68634508140166
Cl	5.25432391149402	1.74689653887681	16.73200053507749
Cl	5.04917296834761	10.35741602459038	13.29099881771655
O	11.52763239651950	8.54517499293920	14.00430082006700
O	11.24287635862684	4.58739806738689	15.12853182820960
H	11.09706789226618	3.77114850564312	15.63269136448578
H	12.20156821071745	4.66902890527886	14.99562048930378

N	11.12636331633291	7.47339158612087	14.14577104934863
N	9.14099445661869	6.95665943062505	16.76489937149579
N	8.27618796272121	4.70280457484002	15.35482035524742
N	8.84950919945358	5.12930773960271	12.74174603742740
N	8.20096719308995	7.36789665791173	14.24700376934679
C	10.19750435922855	6.86816556420673	17.88256886981074
C	11.56083060075713	7.32250407080382	17.34707887329915
H	12.30225062719128	7.25368739413108	18.15577621910916
H	11.56628928299251	8.36576213193318	17.00175216351625
H	11.91281148213394	6.68035315289274	16.52830724604977
C	9.80932134511265	7.74215152286755	19.08561419674407
H	8.81248280849696	7.49566707353682	19.48192972771707
H	9.83509782391830	8.81562772187780	18.84738463242411
H	10.52545816468364	7.57688197673243	19.90345201598601
C	10.32277764429859	5.40346615060907	18.33174673251113
H	11.15268311486615	5.31633135611751	19.04757034983989
H	10.54650387148513	4.74018609615255	17.48675946945682
H	9.42667617911946	5.02628294478352	18.84179322843829
C	7.86881933027266	6.28021633262211	17.15114448898375
H	7.02396570975649	6.90309904247671	16.81559210542083
H	7.75709684290964	6.21791456606883	18.24157206451553
C	7.63907380422419	4.92695756251103	16.51208615671885
C	6.69475376023314	4.01895050481038	16.98415106312754
H	6.17655116023502	4.17622845091721	17.93132387829633
C	6.39460287932496	2.90277034070898	16.18803029684874
C	6.99382841726866	2.75031038754676	14.92327696870972
H	6.69956392954994	1.92616047951554	14.27156971677051
C	7.94334648161946	3.68849420068673	14.53626891086590
C	8.62406151079803	3.72085514945829	13.18036132748701
H	8.01816264425078	3.15415071302466	12.45629334412275
H	9.59946914375231	3.21957118602395	13.24162601714718
C	9.76370928244036	5.24443497237255	11.50820411982309
C	11.19146642245236	4.82001331130571	11.87752092754953
H	11.82536416983108	4.89782038192949	10.98352092804730
H	11.25802634203082	3.77906119821560	12.22531449682729
H	11.63018538131849	5.48031303701436	12.63915695876262
C	9.26204778585709	4.35975324089267	10.35611133573145
H	8.21905928919817	4.57581837847894	10.07851490215550
H	9.34683400926968	3.28662878608837	10.58339876976700
H	9.87470822705111	4.54771902588621	9.46296303610591
C	9.79476566573707	6.71277611047933	11.05511171110114
H	10.05642478899114	7.39485288689071	11.87482731338563
H	8.84400112236083	7.04636750199325	10.61842117325712
H	10.55631701589544	6.83149271236432	10.27152954867876
C	7.53548658267233	5.79803543971667	12.52464398783273
H	6.74581090803946	5.17783355968193	12.97881598690583
H	7.27568777200707	5.85600968606160	11.45938881950484
C	7.40860776799048	7.15329948095159	13.18650818985435
C	6.41933596209043	8.07188783521290	12.84575043925175

H	5.77694633933344	7.91951142970255	11.97713873031086
C	6.24143990968585	9.19051176843667	13.67437516232233
C	7.00945097057638	9.33388790580239	14.84472491102995
H	6.81715580737439	10.16029195304233	15.53046665741486
C	7.99259485799553	8.38624523216719	15.10148319789909
C	8.83980715389339	8.35927718736215	16.35929710243748
H	9.78661970542696	8.88877788475781	16.18279579726332
H	8.31370893354637	8.91310868687466	17.15306921373390

==========

Final structure (after geometry optimization for CASSCF calculation from BAGEL)

==========

Fe	9.706232031	6.099922776	14.686653017
Cl	5.683169488	1.429607324	16.815949590
Cl	4.777926364	10.181730259	13.334477391
O	12.144823025	8.725320712	13.849424128
O	11.489946105	4.819730382	15.070961055
H	11.414766047	4.018435059	15.577400334
H	12.406964222	4.906517809	14.834872302
N	11.440822890	7.847409906	13.966211360
N	9.021245759	6.994464804	16.857565797
N	8.305050445	4.671885362	15.353172499
N	8.799225009	5.142787717	12.668260239
N	8.054872768	7.362610949	14.281791796
C	10.068751756	7.050930692	17.965925227
C	11.375028328	7.646028567	17.426889556
H	12.098167351	7.708420397	18.238052660
H	11.265547578	8.654019434	17.035394453
H	11.815287690	7.013617828	16.656340940
C	9.594151830	7.894051608	19.161099100
H	8.627001948	7.571834259	19.545677175
H	9.527762847	8.953419653	18.919580477
H	10.308952568	7.798421983	19.977207418
C	10.375575364	5.625345392	18.445644933
H	11.239144924	5.651695404	19.106892669
H	10.620764159	4.963632840	17.615694860
H	9.563773634	5.175315724	19.011562589
C	7.856027373	6.157498190	17.231981362
H	6.940348956	6.687060595	16.967093685
H	7.795594589	6.016962680	18.305718801
C	7.731632957	4.806381384	16.539578284
C	6.916904003	3.806501996	17.044049878
H	6.457137512	3.885999348	18.018116190
C	6.673879751	2.698211705	16.239655399
C	7.196815821	2.633496799	14.947136357
H	6.952731292	1.806377634	14.297177528
C	8.016174073	3.664857390	14.536325938
C	8.603800847	3.748039480	13.132641846
H	7.951888274	3.189131633	12.461641648

H	9.562327868	3.236392518	13.126818469
C	9.656383044	5.226650715	11.405520036
C	11.101030612	4.819530807	11.719570731
H	11.691115208	4.878334913	10.806268992
H	11.196837307	3.800200740	12.088051798
H	11.563967370	5.497802157	12.436558423
C	9.118688275	4.316944586	10.288971811
H	8.069493691	4.505853488	10.062613008
H	9.230777389	3.259859798	10.525520251
H	9.679387328	4.499287880	9.373095518
C	9.684884082	6.678918854	10.905304231
H	9.968495556	7.378082548	11.691006985
H	8.738260115	7.007498026	10.484027956
H	10.423417857	6.763667613	10.110617894
C	7.487706653	5.807920613	12.493463023
H	6.707017259	5.164961380	12.901107932
H	7.235257889	5.925106729	11.445356775
C	7.305712593	7.137195400	13.210886550
C	6.282338804	8.003568282	12.867056638
H	5.677607088	7.843909310	11.986647828
C	6.025091166	9.076263622	13.713514221
C	6.746063090	9.225619593	14.898383578
H	6.499886245	10.013781106	15.594741866
C	7.761646659	8.326286161	15.150066485
C	8.565848263	8.342115953	16.441847982
H	9.430640015	8.985848446	16.304005890
H	7.951948715	8.813081329	17.209741283

Supplementary Table S9. Vibrational frequencies (in cm^{-1}) of the optimized structures.

==========

^{2}2

==========

23.70 46.20 74.57 86.78 92.62 96.85 112.63 123.87
133.03 144.87 148.39 149.36 153.94 167.81 175.02
191.93 199.30 209.22 215.47 220.07 222.62 225.65
241.99 245.18 255.78 268.85 274.75 281.73 287.41
291.44 303.58 315.03 323.97 329.04 331.87 345.10
348.98 359.32 375.67 383.00 401.33 406.46 411.93
418.10 438.87 442.04 450.81 461.59 483.46 490.07
494.26 504.57 528.43 533.87 544.45 546.97 558.63
560.57 575.96 576.93 590.17 632.30 644.09 698.05
709.82 727.00 751.07 762.16 786.39 826.81 842.93
872.53 888.99 895.31 898.25 908.10 910.38 927.23
929.59 932.53 937.82 939.06 942.64 959.91 967.43
968.13 970.83 1015.39 1019.16 1031.60 1034.85 1043.53
1046.98 1055.63 1060.06 1064.34 1069.05 1099.71 1102.10
1119.01 1121.50 1186.64 1192.85 1206.71 1211.91 1236.60
1252.52 1253.86 1257.30 1262.14 1273.84 1280.31 1284.41
1307.35 1314.12 1322.74 1329.69 1363.27 1371.10 1381.73
1386.53 1393.48 1399.73 1400.42 1404.69 1423.91 1426.20
1448.57 1451.06 1451.70 1457.27 1457.88 1459.64 1461.57
1462.94 1465.76 1469.29 1473.02 1478.61 1483.62 1486.61
1487.57 1488.45 1491.59 1492.55 1496.09 1498.07 1583.73
1609.83 1614.71 1646.56 1653.07 1887.70 1987.60 3047.39
3048.14 3054.90 3062.28 3065.58 3066.99 3068.87 3074.13
3076.17 3083.37 3128.99 3130.90 3132.46 3134.76 3137.68
3139.52 3140.74 3141.50 3143.70 3144.65 3148.11 3149.06
3149.84 3150.63 3162.51 3179.53 3216.54 3217.52 3218.17
3219.26 3767.70 3850.79

==========

^{4}2

==========

20.80 37.04 55.47 71.80 78.29 85.87 93.01 109.60
110.54 127.60 140.66 144.54 146.64 152.34 173.51
183.69 191.12 198.50 206.40 207.78 214.94 222.92
228.54 234.49 248.50 254.43 265.03 271.35 278.62
285.82 288.11 290.53 302.98 304.27 308.73 319.17
322.91 325.94 343.60 356.16 368.70 377.38 392.84
397.79 409.74 415.32 432.39 447.92 458.28 473.28
477.23 487.50 495.14 504.82 529.66 534.53 541.61
546.21 562.02 564.42 574.64 588.62 632.37 652.90
695.61 708.69 727.25 757.64 779.55 786.81 846.26
847.88 876.65 888.19 895.54 898.62 910.39 913.73
925.61 929.15 935.20 935.66 937.91 949.89 958.67
960.02 970.31 978.71 1015.06 1022.18 1030.78 1038.06
1040.36 1047.88 1053.67 1055.77 1063.70 1067.45 1110.87
1112.64 1120.21 1120.92 1189.69 1192.54 1204.38 1208.70

1250.98 1252.24 1257.31 1257.90 1265.08 1275.30 1284.04
1289.91 1306.90 1313.05 1327.66 1333.58 1366.41 1372.52
1380.92 1388.63 1397.18 1400.10 1400.99 1405.93 1424.52
1426.13 1449.22 1452.27 1454.25 1454.84 1455.92 1457.64
1459.83 1461.94 1463.29 1470.84 1475.79 1477.41 1479.82
1482.85 1485.82 1487.35 1490.75 1491.69 1492.77 1493.40
1608.83 1611.55 1615.63 1645.85 1648.86 1949.33 3047.21
3049.39 3056.42 3058.46 3059.90 3061.61 3066.96 3070.54
3072.28 3072.50 3120.51 3126.11 3127.03 3130.32 3132.52
3134.58 3138.60 3138.63 3141.74 3141.86 3143.87 3147.63
3147.67 3148.16 3165.36 3169.33 3214.16 3214.74 3215.43
3217.04 3758.10 3848.10

==========

^{6}2

==========

16.09 21.67 41.38 53.92 70.63 79.04 81.81 97.54
105.44 108.06 133.97 137.94 145.58 146.41 151.37
163.40 175.91 183.65 194.44 202.56 208.75 213.01
222.22 223.34 227.33 229.84 244.44 255.60 262.69
268.74 273.48 275.34 285.02 289.75 293.24 296.25
309.86 311.66 318.67 324.98 340.89 354.60 371.27
390.25 397.50 409.96 410.71 429.92 448.28 472.46
474.36 486.28 492.69 495.39 529.29 531.33 538.90
546.65 561.61 564.27 574.00 589.11 633.50 652.40
695.71 708.28 726.03 756.69 778.07 785.55 846.83
848.45 876.53 888.05 895.49 898.75 910.06 913.01
925.85 926.33 934.10 935.61 938.76 950.43 956.12
958.21 970.25 978.06 1014.80 1021.97 1029.20 1035.71
1039.85 1048.56 1052.19 1055.15 1064.21 1068.02 1112.66
1114.73 1119.95 1121.04 1191.64 1195.10 1204.01 1208.26
1252.81 1254.20 1256.00 1256.27 1265.05 1275.14 1283.59
1288.80 1306.36 1312.22 1326.69 1333.25 1366.37 1372.56
1380.02 1387.39 1397.44 1398.90 1400.65 1404.35 1424.87
1425.17 1448.98 1450.43 1453.39 1453.86 1455.96 1456.60
1459.28 1461.16 1462.26 1469.52 1475.54 1476.88 1479.01
1482.40 1484.85 1486.46 1490.20 1491.28 1491.67 1492.88
1608.34 1610.52 1613.17 1644.80 1647.53 1949.27 3047.59
3048.21 3053.28 3057.69 3058.10 3059.81 3063.83 3066.80
3068.70 3070.75 3121.74 3122.65 3123.14 3126.93 3130.82
3131.14 3136.92 3137.54 3138.03 3141.69 3142.56 3146.94
3147.66 3149.32 3157.87 3163.44 3214.63 3214.67 3215.13
3216.67 3754.17 3840.46

VI. References

1. Kim, K., Oh, S., Jeong, D., Lee, Y., Moon, D., Lee, S. & Cho, J. Systematic electronic tuning on the property and reactivity of cobalt–(hydro)peroxo intermediates. *Inorg. Chem.* **62**, 7141–7149 (2023).
2. Evans, D. 400. The determination of the paramagnetic susceptibility of substances in solution by nuclear magnetic resonance. *J. Chem. Soc.* (Resumed), 2003-2005 (1959).
3. Loliger, J. & Scheffold, R. Paramagnetic moment measurements by nmr. a micro technique. *J. Chem. Educ.* **49**, 646 (1972).
4. Kumar, P. et al. Reactions of Co(III)–nitrosyl complexes with superoxide and their mechanistic insights. *J. Am. Chem. Soc.* **137**, 4284–4287 (2015).
5. Kumar, P., Lee, Y.-M., Park, Y. J., Siegler, M. A., Karlin, K. D. & Nam, W. Factors that control the reactivity of cobalt(III)–nitrosyl complexes in nitric oxide transfer and dioxygenation reactions: a combined experimental and theoretical investigation. *J. Am. Chem. Soc.* **138**, 7753–7762 (2016).
6. Shin, J. W., Eom, K. & Moon, D. BL2D-SMC, the supramolecular crystallography beamline at the Pohang Light Source II, Korea. *J. Synchrotron Radiat.* **23**, 369–373 (2016).
7. Otwinowski, Z. & Minor, W. Processing of X-ray diffraction data collected in oscillation mode. *Methods Enzymol.* **276**, 307–326 (1997).
8. Sheldrick, G. M. SHELXT – Integrated space-group and crystal-structure determination. *Acta Crystallogr. Sect. Found. Adv*. **71**, 3–8 (2015).
9. Sheldrick, G. M. Crystal structure refinement with SHELXL. *Acta Crystallogr. C Struct. Chem.* **71**, 3–8 (2015).
10. Khusnutdinova, J. R., Luo, J., Rath, N. P. & Mirica, L. M. Late first-row transition metal complexes of a tetradentate pyridinophane ligand: electronic properties and reactivity implications. Inorg. Chem. 52, 3920–3932 (2013).
11. Parr, R. G. & Weitao, Y. *Density-Functional Theory of Atoms and Molecules*. (Oxford University Press, 1994).
12. Neese, F., Wennmohs, F., Becker, U. & Riplinger, C. The ORCA quantum chemistry program package. *J. Chem. Phys.* **152**, 224108 (2020).
13. Slater, J. C. *The Self-Consistent Field for Molecules and Solids: Quantum Theory of Molecules and Solids*. (McGraw-Hill Book Company, 1974).

14. Vosko, S. H., Wilk, L. & Nusair, M. Accurate spin-dependent electron liquid correlation energies for local spin density calculations: a critical analysis. *Can. J. Phys.* **58**, 1200–1211 (1980).
15. Becke, A. D. Density-functional exchange-energy approximation with correct asymptotic behavior. *Phys. Rev. A Gen. Phys.* **38**, 3098–3100 (1988).
16. Lee, C., Yang, W. & Parr, R. G. Development of the Colle-Salvetti correlation-energy formula into a functional of the electron density. *Phys. Rev. B* **37**, 785–789 (1988).
17. Becke, A. D. Density-functional thermochemistry. III. The role of exact exchange. *J. Chem. Phys.* **98**, 5648–5652 (1993).
18. Grimme, S., Antony, J., Ehrlich, S. & Krieg, H. A consistent and accurate ab initio parametrization of density functional dispersion correction (DFT-D) for the 94 elements H-Pu. *J. Chem. Phys.* **132**, 154104 (2010).
19. Weigend, F. & Ahlrichs, R. Balanced basis sets of split valence, triple zeta valence and quadruple zeta valence quality for H to Rn: Design and assessment of accuracy. *Phys. Chem. Chem. Phys.* **7**, 3297–3305 (2005).
20. Dunlap, B. I., Connolly, J. W. D. & Sabin, J. R. On some approximations in applications of Xα theory. *J. Chem. Phys.* (1979).
21. Vahtras, O., Almlöf, J. & Feyereisen, M. W. Integral approximations for LCAO-SCF calculations. *Chem. Phys. Lett.* **213**, 514–518 (1993).
22. Neese, F., Wennmohs, F., Hansen, A. & Becker, U. Efficient, approximate and parallel Hartree–Fock and hybrid DFT calculations. A 'chain-of-spheres' algorithm for the Hartree–Fock exchange. *Chem. Phys.* **356**, 98–109 (2009).
23. Izsák, R. & Neese, F. An overlap fitted chain of spheres exchange method. *J. Chem. Phys.* **135**, 144105 (2011).
24. Izsák, R., Neese, F. & Klopper, W. Robust fitting techniques in the chain of spheres approximation to the Fock exchange: The role of the complementary space. *J. Chem. Phys.* **139**, 094111 (2013).
25. Weigend, F. Accurate Coulomb-fitting basis sets for H to Rn. *Phys. Chem. Chem. Phys.* **8**, 1057–1065 (2006).
26. Barone, V. & Cossi, M. Quantum calculation of molecular energies and energy gradients in solution by a conductor solvent model. *J. Phys. Chem. A* **102**, 1995–2001 (1998).

27. Garcia-Ratés, M. & Neese, F. Effect of the solute cavity on the solvation energy and its derivatives within the framework of the Gaussian charge scheme. *J. Comput. Chem.* **41**, 922–939 (2020).
28. Veryazov, V., Malmqvist, P. Å. & Roos, B. O. How to select active space for multiconfigurational quantum chemistry? *Int. J. Quantum Chem.* **111**, 3329–3338 (2011).
29. Pierloot, K. The CASPT2 method in inorganic electronic spectroscopy: from ionic transition metal to covalent actinide complexes∗. *Mol. Phys.* **101**, 2083–2094 (2003).
30. Pettersen, E. F. *et al.* UCSF Chimera--a visualization system for exploratory research and analysis. *J. Comput. Chem.* **25**, 1605–1612 (2004).
31. Shiozaki, T. BAGEL: Brilliantly advanced general electronic-structure library. *Wiley Interdiscip. Rev. Comput. Mol. Sci.* **8**, e1331 (2018).
32. Maji, R. C., Barman, S. K., Roy, S., Chatterjee, S. K., Bowles, F. L., Olmstead, M. M. & Patra, A. K. Copper complexes relevant to the catalytic cycle of copper nitrite reductase: electrochemical detection of NO(*g*) evolution and flipping of NO_2 binding mode upon $Cu^{II} \rightarrow Cu^{I}$ reduction. *Inorg. Chem.* **52**, 11084–11095 (2013).